

# Chiral anomaly of Weyl magnons in stacked honeycomb ferromagnets

Ying Su<sup>1,2</sup> and X. R. Wang<sup>1,2\*</sup>

<sup>1</sup>Physics Department, The Hong Kong University of Science and Technology, Clear Water Bay, Kowloon, Hong Kong and

<sup>2</sup>HKUST Shenzhen Research Institute, Shenzhen 518057, China

(Dated: May 12, 2017)

Chiral anomaly of Weyl magnons (WMs), featured by nontrivial band crossings at paired Weyl nodes (WNs) of opposite chirality, is investigated. It is shown that WMs can be realized in stacked honeycomb ferromagnets. Using the Aharonov-Casher effect that is about the interaction between magnetic moments and electric fields, the magnon motion in honeycomb layers can be quantized into magnonic Landau levels (MLLs). The zeroth MLL is chiral so that unidirectional WMs propagate in the perpendicular (to the layer) direction for a given WN under a magnetic field gradient from one WN to the other and change their chiralities, resulting in the magnonic chiral anomaly (MCA). A net magnon current carrying spin and heat through the zeroth MLL depends linearly on the magnetic field gradient and the electric field gradient in the ballistic transport.

PACS numbers:

Topological magnetic states have attracted enormous attention in recent years [1–23], because of their fundamental interest and importance in magnonics that is about generation, detection, and manipulation of magnons [24–27]. Magnons, the quanta of low-energy excitations of magnetic materials, can carry, process, and transmit information [28, 29] like electrons besides being a control knob of magnetization dynamics [30–32]. So far, almost all studies on Weyl magnons (WMs) focus on the nontrivial band topology of Weyl nodes (WNs) and magnon surface states in pyrochlore magnetic materials [19–21]. There is no study of magnonic chiral anomaly (MCA), one of the two important signatures of Weyl materials [the other is the magnon (Fermi) arc on sample surfaces due to topologically protected surface states between two paired WNs]. The realization and detection of the MCA are the main theme of this work.

To study the MCA, one needs to have three-dimensional (3D) Weyl magnetic materials and to realize the magnonic Landau levels (MLLs) first. Only then one can study the magnon transport through the zeroth MLL under driving forces, i.e. the MCA. WNs in Weyl magnetic materials appear usually at high energy [19–21]. Thus, it is not trivial to inject magnons into the high-energy WNs to create WMs. In this paper, we show that stacked honeycomb ferromagnets can be a Weyl magnetic material that supports both type-I WMs and type-II WMs. A two-band model is found with either one pair or two pairs of WNs. Magnons can interact with electric fields through the Aharonov-Casher effect [33] so that magnon motion in honeycomb layers can be quantized into the MLLs by a proper inhomogeneous electric field. A quasi-one-dimensional magnon conductor connected to two magnon reservoirs under a proper inhomogeneous magnetic field perpendicular to the honeycomb layers is used to study the MCA and magnon transport

in the longitudinal direction.

Our 3D WMs exist in stacked honeycomb ferromagnets as shown in Fig. 1(a). The honeycomb lattices (in the  $xy$  plane) are perfectly aligned in the  $z$  direction. A spin  $\mathbf{S}$  (in units of  $\hbar$ ) polarized in the  $z$  direction is on each site.  $\mathbf{a}_i$  (red arrows) and  $\mathbf{b}_i$  (green arrows) ( $i = 1, 2, 3$ ) defined in honeycomb layers are three vectors connecting nearest neighbor (NN) sites and three vectors connecting next nearest neighbor (NNN) sites, respectively [34]. A and B denote two sublattices of honeycomb layers. The layer separation is the same as the distance between two NN intralayer lattice sites that is set as unity. The spin Hamiltonian reads

$$H = -J \sum_{\langle i,j \rangle, l} \mathbf{S}_{i,l} \cdot \mathbf{S}_{j,l} - \sum_{i,l} K_i S_{i,l}^z - \sum_{i, \langle l, l' \rangle} J_i \mathbf{S}_{i,l} \cdot \mathbf{S}_{i,l'} + D \sum_{\langle\langle i,j \rangle\rangle, l} \nu_{ij} \hat{\mathbf{z}} \cdot (\mathbf{S}_{i,l} \times \mathbf{S}_{j,l}) - g\mu_B B_0 \sum_{i,l} S_{i,l}^z, \quad (1)$$

where  $i$  and  $j$  label lattice sites in honeycomb layers, and  $l$  and  $l'$  are layer indexes.  $\langle i, j \rangle$  and  $\langle\langle i, j \rangle\rangle$  denote the NN and NNN intralayer sites, and  $\langle l, l' \rangle$  are the NN layers. The first term describes the NN intralayer ferromagnetic exchange interaction with  $J > 0$ . The second term is the anisotropy energy with easy axis along  $z$  direction and anisotropy coefficients  $K_i = K_A$  ( $K_B$ ) for sites on sublattice A (B).  $J_i = J_A$  ( $J_B$ ) in the third term are the NN interlayer exchange coefficients for sites on sublattice A (B). The fourth term describes the Dzyaloshinskii-Moriya interaction [14–17, 35] and  $\nu_{ij} = (2/\sqrt{3})(\hat{\mathbf{d}}_1 \times \hat{\mathbf{d}}_2)_z = \pm 1$ , where  $\hat{\mathbf{d}}_1$  and  $\hat{\mathbf{d}}_2$  are the unit vectors along NN intralayer bonds connecting the common NN site of  $i$  and  $j$  to site  $j$  and  $i$ . The last term is the Zeeman energy due to the external magnetic field  $B_0$  along  $z$  direction ( $B_0 = 0$  is assumed below since it only shifts the energy).

Under the Holstein-Primakoff transformation  $S_{i,l}^+ = \sqrt{2S - n_{i,l}} c_{i,l}$ ,  $S_{i,l}^- = c_{i,l}^\dagger \sqrt{2S - n_{i,l}}$ ,  $n_{i,l} = c_{i,l}^\dagger c_{i,l}$  [36], where  $c_{i,l}^\dagger$  and  $c_{i,l}$  are magnon creation and annihilation

\*corresponding author: phxwan@ust.hk

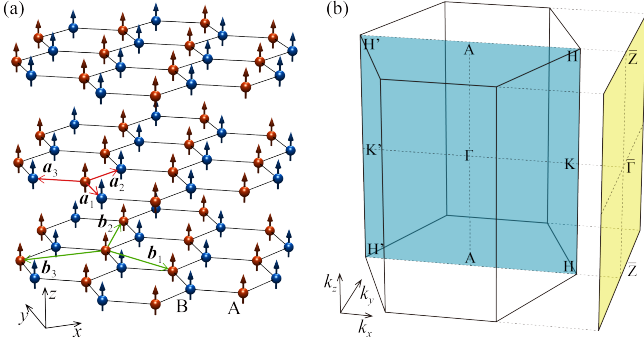


FIG. 1: (color online). (a) Schematic diagram of stacked honeycomb ferromagnets. Each site has a spin of  $\mathbf{S}$  polarized in the  $z$  direction, represented by a red dot with an arrow on sublattice A and a blue dot with an arrow on sublattice B. The in-plane vectors  $\mathbf{a}_{1(2,3)}$  and  $\mathbf{b}_{1(2,3)}$  are explained in the text. (b) The first bulk Brillouin zone (BZ) and the first (100) surface BZ of the stacked honeycomb ferromagnets.

operators satisfying the boson commutation relations, Hamiltonian (1) becomes a tight-binding Hamiltonian

$$H = -JS \sum_{\langle i,j \rangle, l} (c_{i,l}^\dagger c_{j,l} + \text{H.c.}) - DS \sum_{\langle\langle i,j \rangle\rangle, l} (i\nu_{ij} c_{i,l}^\dagger c_{j,l} + \text{H.c.}) + \sum_{i,l} V_i c_{i,l}^\dagger c_{i,l} - \sum_{i,\langle l,l' \rangle} J_i S (c_{i,l}^\dagger c_{i,l'} + \text{H.c.}), \quad (2)$$

where  $V_i = 3JS + 2K_i S + 2J_i S$  is the sublattice-dependent on-site energy. The Hamiltonian can be block diagonalized in momentum space as  $H = \sum_{\mathbf{k}} c_{\mathbf{k}}^\dagger \mathcal{H}(\mathbf{k}) c_{\mathbf{k}}$ , where  $c_{\mathbf{k}} = (a_{\mathbf{k}}, b_{\mathbf{k}})^T$  and  $\mathcal{H}(\mathbf{k}) = \varepsilon_0(\mathbf{k})I + \sum_{\beta} h_{\beta}(\mathbf{k})\sigma_{\beta}$ , ( $\beta = x, y, z$ ).  $a_{\mathbf{k}}$  and  $b_{\mathbf{k}}$  are respectively defined on sublattices A and B.  $I$ ,  $\sigma_x$ ,  $\sigma_y$ , and  $\sigma_z$  are the  $2 \times 2$  identity matrix, and three Pauli matrices. The other quantities are  $\varepsilon_0(\mathbf{k}) = 3JS + K_+ S + J_+ S(1 - \cos k_z)$ ,  $h_x(\mathbf{k}) = -JS \sum_{j=1}^3 \cos(\mathbf{k} \cdot \mathbf{a}_j)$ ,  $h_y = -JS \sum_{j=1}^3 \sin(\mathbf{k} \cdot \mathbf{a}_j)$ ,  $h_z(\mathbf{k}) = 2DS \sum_{j=1}^3 \sin(\mathbf{k} \cdot \mathbf{b}_j) + K_- S + J_- S(1 - \cos k_z)$ ,  $K_{\pm} = K_A \pm K_B$  and  $J_{\pm} = J_A \pm J_B$ . The dispersion relations of the two magnon bands are  $\varepsilon_{\pm}(\mathbf{k}) = \varepsilon_0(\mathbf{k}) \pm \sqrt{\sum_{\beta} h_{\beta}^2(\mathbf{k})}$ .

The two magnon bands cross at  $\mathbf{k}$  called a WN when  $h_{x(y,z)}(\mathbf{k}) = 0$ . This may happen on two lines, HKH and H'K'H', in the first Brillouin zone (BZ) shown in Fig. 1(b) because  $h_{x(y)}(\mathbf{k}) = 0$  and  $h_z(\mathbf{k}) = \pm 3\sqrt{3}DS + K_- S + J_- S(1 - \cos k_z)$  for  $\mathbf{k} = (\pm 4\pi/3\sqrt{3}, 0, k_z)$ . WNs are located at  $\mathbf{k}_1^{\pm} = (-4\pi/3\sqrt{3}, 0, \pm \cos^{-1} f_1)$  on H'K'H' and at  $\mathbf{k}_2^{\pm} = (4\pi/3\sqrt{3}, 0, \pm \cos^{-1} f_2)$  on HKH, where  $f_{\eta} = K_-/J_- + 1 + (-1)^{\eta} 3\sqrt{3}D/J_-$  ( $\eta = 1, 2$ ). Conditions of  $|f_{\eta}| \leq 1$  result in four phase boundary lines of  $K_- = \pm 3\sqrt{3}D$  (solid lines) and  $K_- + 2J_- = \pm 3\sqrt{3}D$  (dashed lines) in Fig. 2(a), that divide the  $J_-/D$ - $K_-/D$  plane into nine regions (colored differently). The two magnon bands are gapped in both white and green regions. However, the system in the green region is in a topologically nontrivial phase in which topologically protected surface states exist in the band gap (see Supple-

mental Material Ref. [37]). This phase is called topological magnon insulator in the literature [5]. For an arbitrary  $k_z$ , Hamiltonian  $\mathcal{H}_{k_z}(k_x, k_y)$  gives a nonzero Chern number [37]. On the other hand, the system in the white regions is in a trivial phase with zero topological number.

The rest of regions in Fig. 2(a) belongs to three different WM phases: the WM in the pink regions has one pair of WNs at  $\mathbf{k}_1^{\pm}$ ; WMs in the yellow regions has one pair of WNs at  $\mathbf{k}_2^{\pm}$ ; and WMs in the purple regions has two pairs of WNs at  $\mathbf{k}_1^{\pm}$  and  $\mathbf{k}_2^{\pm}$ . The effective Weyl Hamiltonian (to the first order in the momentum deviation  $\mathbf{q} = \mathbf{k} - \mathbf{k}_{\eta}^{\pm}$ ) around the WNs  $\mathbf{k}_{\eta}^{\pm}$  can be obtained from the Taylor expansion as

$$\mathcal{H}_{\eta}^{\pm}(\mathbf{q}) = (\varepsilon_{\eta} + \hbar u_{\eta,z}^{\pm} q_z)I + \sum_{\beta=x,y,z} \hbar v_{\eta,\beta}^{\pm} q_{\beta} \sigma_{\beta}, \quad (3)$$

where  $\varepsilon_{\eta} = 3JS + K_+ S + J_+ S(1 - f_{\eta})$ ,  $u_{\eta,z}^{\pm} = \pm J_+ S \sqrt{1 - f_{\eta}^2/\hbar}$ ,  $v_{\eta,x}^{\pm} = (-1)^{\eta} 3JS/2\hbar$ ,  $v_{\eta,y}^{\pm} = 3JS/2\hbar$ , and  $v_{\eta,z}^{\pm} = \pm J_- S \sqrt{1 - f_{\eta}^2/\hbar}$ . The chirality of WNs at  $\mathbf{k}_{\eta}^{\pm}$  can be calculated from the effective Weyl Hamiltonian Eq. (3) as  $\chi_{\eta}^{\pm} = \text{sgn}(\prod_{\beta} v_{\eta,\beta}^{\pm}) = \pm(-1)^{\eta} \text{sgn}(J_-)$  [38]. Thus WNs appear in pairs with opposite chirality as required by the no-go theorem [38–40]. According to the classification of Weyl semimetals [41], the WMs are of type-II when  $|u_{\eta,z}^{\pm}| > |v_{\eta,z}^{\pm}| \Rightarrow |J_+| > |J_-|$  (see Supplemental Material Ref. [37]). Namely,  $J_A$  and  $J_B$  have the same sign. Otherwise the WMs are of type-I. Two WNs  $\mathbf{k}_1^{\pm}$  merge at K' on boundary  $K_- = 3\sqrt{3}D$  (blue solid line) and at H' on boundary  $K_- + 2J_- = 3\sqrt{3}D$  (blue dash line), while two WNs  $\mathbf{k}_2^{\pm}$  merge at K on boundary  $K_- = -3\sqrt{3}D$  (red solid line) and at H on boundary  $K_- + 2J_- = -3\sqrt{3}D$  (red dash line). At  $(K_-/D, J_-/D) = (-3\sqrt{3}, 0)$  and  $(3\sqrt{3}, 0)$ , WMs become nodal-line magnons [22] in which two magnon bands cross on HKH line for the former and on H'K'H' line for the later (see Supplemental Material Ref. [37]).

One can use energy surfaces of two magnon bands, say as a function of  $k_x$  and  $k_z$  for fixed  $k_y = 0$  [the blue plane in Fig. 1(b)], to visualize the WNs of WMs identified above. To be concrete and without losing generality, we set  $D = 0.2J$ ,  $K_+ = 12D$ , and  $J_+ = 2D$  below. The magnon bands for  $(K_-, J_-) = (D, 5D)$  and  $(-9D, 9D)$  [respectively marked by the black and white dots in Fig. 2(a)] are plotted in Fig. 2(b) and 2(c). Apparently, they are type-I WMs with one or two pairs of WNs denoted by the red and blue dots for chirality  $\pm 1$ , respectively. The magnon bands for type-II and nodal-line magnons are shown in the Supplemental Material Ref. [37]. The WM phase can also be confirmed by the topological number calculations from the Berry curvature  $\Omega_{\pm}(\mathbf{k}) = i\nabla_{\mathbf{k}} \times (\pm, \mathbf{k}|\nabla_{\mathbf{k}}|_{\pm}, \mathbf{k})$ , where  $|\pm, \mathbf{k}\rangle$  are the eigenstates of the upper and lower magnon bands, and  $\Omega_+(\mathbf{k}) = -\Omega_-(\mathbf{k})$ . From the effective Weyl Hamiltonian Eq. (3), the Berry curvature of the lower magnon band

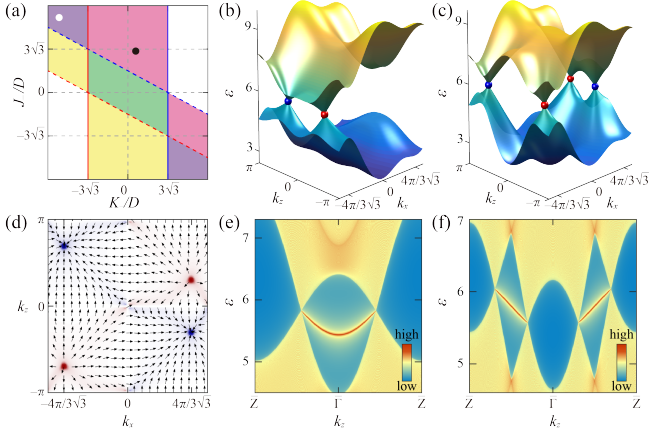


FIG. 2: (color online). (a) Phase diagram in the  $K_-/D$ - $J_-/D$  plane divided by four boundaries  $K_- = \pm 3\sqrt{3}D$  and  $K_- + 2J_- = \pm 3\sqrt{3}D$ . The yellow, pink, and purple regions denote three different WM phases. The system is in the topological magnon insulator phase in the green region while it is the trivial gapped phase in the white region. The black and white dots correspond to the magnon band structures in (b) and (c) whose model parameters are specified in the text. The Weyl nodes of chirality  $\pm 1$  are marked by red and blue dots. (d) The Berry curvature of the lower magnon band in (c). The arrows represent the direction of Berry curvature vectors in the  $k_x k_z$  plane with  $k_y = 0$ . The background color denotes the divergence of Berry curvature, where red and blue represent positive and negative values, respectively. (f) and (e) The density plot of (100) surface spectral functions for the magnon bands in (b) and (c). Energy  $\varepsilon$  is in units of  $JS$ , and insets are the colorbars.

around the WN at  $\mathbf{k}_\eta^\pm$  can be analytically calculated

$$\Omega_-(\mathbf{k}_\eta^\pm + \mathbf{q}) = \frac{\prod_\beta v_{\eta,\beta}^\pm \mathbf{q}}{2 \left( \sum_\beta v_{\eta,\beta}^{\pm 2} q_\beta^2 \right)^{3/2}}, \quad (4)$$

which diverges at the WN (where  $\mathbf{q} = 0$ ), corresponding to a magnetic monopole there in the momentum space as shown in Fig. 2(d) that is the numerical result of the exact Hamiltonian  $\mathcal{H}(\mathbf{k})$  for the lower magnon band in Fig. 2(c) with  $k_y = 0$ . The black arrows show the directions of the projection of Berry curvature onto the  $k_x k_z$  plane and the color represents the divergence of Berry curvature  $\nabla_{\mathbf{k}} \cdot \Omega_-(\mathbf{k})$ : red for positive and blue for negative. Thus, the red and blue spots in Fig. 2(d) correspond to the WNs in Fig. 2(c).

The monopole charge carried by the WN at  $\mathbf{k}_\eta^\pm$  is  $(1/2\pi) \iint_s \Omega_-(\mathbf{k}) \cdot d\mathbf{s}(\mathbf{k}) = \text{sgn}(\prod_\beta v_{\eta,\beta}^\pm) = \chi_\eta^\pm$ , the chiralities of WNs. The integral is on a closed surface  $s$  enclosing the WN in momentum space. The monopole charge is also identical to the Chern number of the lower magnon band on this surface. Thus topologically protected surface states exist between WNs. To see the surface states, we consider a slab whose two end surfaces are perpendicular to the  $[100]$  direction. The (100) surface BZ is represented by the yellow plane in Fig. 1(b), where the projection of the high symmetry points of the first bulk BZ onto the first surface BZ are denoted by the barred symbols. The density plot of the spectral function on the top surface along the  $\bar{Z}\Gamma\bar{Z}$  line (a projection of both H'K'H' and HKH) are shown in Fig. 2(e) and

2(f) for the model parameters used in Fig. 2(b) and 2(c), respectively. The surface states with high density (red color) on the top surface between WNs can be clearly seen. Near the energy of WNs, these surface states form magnon arcs (an analogue of the Fermi arcs) on the sample surfaces, see Supplemental Material Ref. [37].

According to the Aharonov-Casher effect [33], a magnon with a magnetic moment  $\boldsymbol{\mu} = g\mu_B \hat{\mathbf{z}}$  interacts with an electric field  $\mathbf{E} = (\mathcal{E}x, 0, 0)$ . Compare the Aharonov-Casher phase  $\phi_{ij} = (1/\hbar c^2) \int_j^i (\mathbf{E} \times \boldsymbol{\mu}) \cdot d\mathbf{r}$ . This effect is reminiscent of the magnetic field effect on electrons that induces the Aharonov-Bohm phase and leads to the Landau levels. Indeed, the effect has already been used to generate the MLLs and magnonic quantum Hall effect [42]. Here we consider magnons under an inhomogeneous electric field  $\mathbf{E} = (\mathcal{E}x, 0, 0)$ . Compare the Aharonov-Casher phase  $\phi_{ij} = (g\mu_B/\hbar c^2) \int_i^j \mathcal{E}x dy$  for magnons with the usual Aharonov-Bohm phase for electrons, the lattice momentum in the effective Weyl Hamiltonian Eq. (3) should be replaced by  $-i\hbar\nabla + g\mu_B \mathcal{E}x \hat{\mathbf{y}}/c^2$  [42]. The effective Weyl Hamiltonian in the electric field can be solved exactly and the magnon motion in the  $xy$  plane is quantized into the MLLs with the eigenvalues

$$\begin{aligned} \varepsilon_{\eta,n \geq 1}^\pm(q_z) &= \varepsilon_\eta + \hbar u_{\eta,z}^\pm q_z \pm \hbar \sqrt{\lambda_\eta n + v_{\eta,z}^{\pm 2} q_z^2}, \\ \varepsilon_{\eta,0}^\pm(q_z) &= \varepsilon_\eta + \hbar u_{\eta,z}^\pm q_z - (-1)^\eta \text{sgn}(\mathcal{E}) \hbar v_{\eta,z}^\pm q_z, \end{aligned} \quad (5)$$

where  $\lambda_\eta = 2|v_{\eta,x}^\pm v_{\eta,y}^\pm|/l_\mathcal{E}^2$  and electric length  $l_\mathcal{E} = \sqrt{\hbar c^2/g\mu_B |\mathcal{E}|}$  is an analogue of magnetic length for electrons [42]. The MLL degeneracy is  $D = L_x L_y / 2\pi l_\mathcal{E}^2 \propto |\mathcal{E}|$ , where  $L_x$  and  $L_y$  are the sample lengths in  $x$  and  $y$  directions. The zeroth MLL  $\varepsilon_{\eta,0}^\pm(q_z)$  is chiral and linearly dispersed with opposite group velocities  $v_{\eta,g}^\pm = u_{\eta,z}^\pm - (-1)^\eta \text{sgn}(\mathcal{E}) v_{\eta,z}^\pm$  around two paired WNs at  $\mathbf{k}_\eta^\pm$ , where the density of states is  $\rho_\eta = (2\pi^2 l_\mathcal{E}^2 \hbar |v_{\eta,g}^\pm|)^{-1}$  (with the Landau degeneracy included). We also include the Aharonov-Casher phase into the tight-binding Hamiltonian (2) through the Peierls substitution [43] and calculate its spectrum for an infinite long bar along  $z$  direction with periodic boundary condition in  $x$  and  $y$  directions. For the electric field gradient  $\mathcal{E} = 1/150\sqrt{3}$  in units of  $\hbar c^2/g\mu_B$ , the MLLs for the same model parameters used

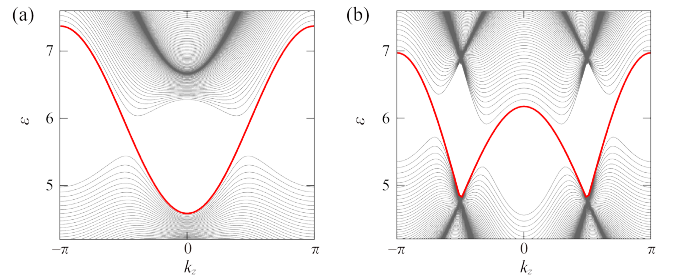


FIG. 3: (color online). (a) and (b) Magnonic Landau levels under an electric field gradient of  $\mathcal{E} = 1/150\sqrt{3}$  (in units of  $\hbar c^2/g\mu_B$ ) for the model parameters identical to those in Fig. 2(b) and 2(c), respectively. The zeroth magnonic Landau levels are the red curves and the energy  $\varepsilon$  is in units of  $JS$ .

in Fig. 2(b) and 2(c) are shown in Fig. 3(a) and 3(b), where the zeroth MLLs are the red curves. The MLLs for type-II WMs are shown in the Supplemental Material Ref. [37].

To realize the MCA, one needs to drive magnons to flow in the direction perpendicular to the magnon quantization plane. Due to the interaction energy  $-\mathbf{B} \cdot \boldsymbol{\mu}$  between a magnetic field  $\mathbf{B}$  and a magnetic moment  $\boldsymbol{\mu}$ , an inhomogeneous magnetic field of  $\mathbf{B} \parallel \boldsymbol{\mu}$  can exert a force of  $g\mu_B \partial_z B_z$  on a magnon so that magnon momentum shall follow the dynamical equation  $\hbar dk_z/dt = g\mu_B \partial_z B_z$ . The change of the magnon momentum drives magnons to flow from one WN to the other due to the unidirectional nature of the zeroth MLL. The transport of chiralities through the zeroth MLL leads to the non-conservation of chirality [39, 44], an important feature of MCA.

To detect the MCA, we can consider a two-terminal setup sketched in Fig. 4 under an inhomogeneous magnetic field along the  $z$  direction. Here a quasi-one-dimensional magnon conductor described by Eq. (1) and in an inhomogeneous electric field described above is connected to two magnon reservoirs. Higher magnetic fields  $B_1$  and  $B_2$  are applied on the reservoirs to shift the magnon band bottom to  $\varepsilon_\eta - g\mu_B \Delta B/2$  and  $\varepsilon_\eta + g\mu_B \Delta B/2$  (where  $\Delta B = B_2 - B_1$ ) so that the system is at nonequilibrium. The imbalance of magnon concentrations between the two reservoirs within the energy window  $[\varepsilon_\eta - g\mu_B \Delta B/2, \varepsilon_\eta + g\mu_B \Delta B/2]$  drives magnons to flow from the left to the right through the magnon conductor [42]. In the ballistic regime where the sample length is smaller than the magnon mean free path, and for a type-I WM with only one pair of WNs at  $\mathbf{k}_\eta^\pm$  ( $\eta = 1$  or 2), the spin and heat currents through the zeroth MLL can be calculated from the Landauer-Büttiker approach [42] as

$$\begin{aligned} I_{s,\eta} &= \int_{\varepsilon_\eta - g\mu_B \Delta B/2}^{\varepsilon_\eta + g\mu_B \Delta B/2} \frac{\hbar L_x L_y n_B(\varepsilon) d\varepsilon}{4\pi^2 l_\xi^2 \hbar} = G_{s,\eta} \Delta B, \\ I_{h,\eta} &= \int_{\varepsilon_\eta - g\mu_B \Delta B/2}^{\varepsilon_\eta + g\mu_B \Delta B/2} \frac{\varepsilon L_x L_y n_B(\varepsilon) d\varepsilon}{4\pi^2 l_\xi^2 \hbar} = G_{h,\eta} \Delta B, \\ G_{s,\eta} &= \frac{L_x L_y g\mu_B n_B(\varepsilon_\eta)}{4\pi^2 l_\xi^2}, \quad G_{h,\eta} = \frac{L_x L_y g\mu_B \varepsilon_\eta n_B(\varepsilon_\eta)}{4\pi^2 l_\xi^2 \hbar}, \end{aligned} \quad (6)$$

where  $n_B(\varepsilon) = (e^{\varepsilon/k_B T} - 1)^{-1}$  is the Bose-Einstein distribution,  $G_{s,\eta}$  and  $G_{h,\eta}$  are respective the spin and heat conductance (from the pair of WNs labeled by  $\eta$ ) in linear response. The neglect of the contributions from higher MLLs ( $n \geq 1$ ) can be justified when  $g\mu_B \Delta B \ll 2\hbar\sqrt{\lambda_\eta}$  such that the energy window is within the energy gap between the first MLLs  $\varepsilon_{\eta,1}^\pm(q_z)$ . Apparently, the spin (heat) conductance is linear in the electric field gradient  $G_{s(h),\eta} \propto l_\xi^{-2} \propto |\mathcal{E}|$  due to the MLL degeneracy. Therefore, the MCA results in positive and linear electric spin (heat) conductance, or negative electric spin (heat) resistance as  $R_{s(h),\eta} \propto |\mathcal{E}|^{-1}$ . These results are experimentally detectable [45] and can be used as the signatures of



FIG. 4: (color online). Schematic diagram of a two-terminal setup under an inhomogeneous magnetic field along  $z$  direction, in which the middle quasi-one-dimensional magnon conductor is connected to two magnon reservoirs.

MCA.

Before concluding this paper, we would like to make the following remarks. 1) The above results should be valid for any number of pairs of nearly degenerate WNs as long as the WM is type-I because each pair of WNs gives one zeroth MLL and different zeroth MLLs are additive. Thus, the total spin (heat) conductance is simply  $G_{s(h)} \simeq \sum_\eta G_{s(h),\eta}$ , due to different pairs of WNs labeled by  $\eta$ . The transport of type-II WMs can be complicated because their higher MLL channels also conduct magnons so that the zeroth MLL cannot be isolated from higher MLLs, see Supplemental Material Ref.[37]. The linear electric spin and heat conductance from MCA means that the electric field gradient can be used to control magnon transport, and this should open a new avenue for magnonics. For diffusive transport (when sample length is much larger than the mean free path), the electric field dependence of spin (heat) conductance should be sensitive to the detailed scattering processes. In fact, it was recently shown that the linear magnetoconductance can exist in disordered Weyl semimetals [46]. How does it work for WMs is an open question for future investigation. 2) Besides the transport measurement, one can also study the WMs by examining WNs and magnon arcs detectable by inelastic neutron scattering that was successfully used to probe the magnon bands of a topological magnon insulator [12]. 3) There is clear difference between the MCA and its electronic counterpart, electronic chiral anomaly. Instead of the electric and magnetic fields parallel to each other, the inhomogeneous electric and magnetic fields in MCA must be perpendicular to each other.

In conclusion, the stacked honeycomb ferromagnets can support both type-I and type-II WMs. MLLs can be realized by the interaction between electric field and magnon magnetic moment through the Aharonov-Casher effect. MCA results in linear dependence of spin and heat conductance on the electric field gradient when mutually perpendicular inhomogeneous electric and magnetic fields are applied. Our results provide a new way to probe WMs and open a door to new electrically controlled magnonic devices.

### Acknowledgments

This work is supported by the NSF of China Grant (No. 11374249) and Hong Kong RGC Grants (No.

163011151 and No. 16301816).

- 
- [1] S. Fujimoto, Phys. Rev. Lett. **103**, 047203 (2009).
- [2] H. Katsura, N. Nagaosa, and P. A. Lee, Phys. Rev. Lett. **104**, 066403 (2010).
- [3] Y. Onose, T. Ideue, H. Katsura, Y. Shiomi, N. Nagaosa, and Y. Tokura, Science **329**, 297 (2010).
- [4] R. Matsumoto and S. Murakami, Phys. Rev. Lett. **106**, 197202 (2011); R. Matsumoto, R. Shindou, and S. Murakami, Phys. Rev. B **89**, 054420 (2014).
- [5] L. Zhang, J. Ren, J.-S. Wang, and B. Li, Phys. Rev. B **87**, 144101 (2013).
- [6] R. Shindou, J. I. Ohe, R. Matsumoto, S. Murakami, and E. Saitoh, Phys. Rev. B **87**, 174402 (2013); R. Shindou, R. Matsumoto, S. Murakami, and J. I. Ohe, Phys. Rev. B **87**, 174427 (2013).
- [7] M. Mochizuki, X. Z. Yu, S. Seki, N. Kanazawa, W. Koshibae, J. Zang, M. Mostovoy, Y. Tokura and N. Nagaosa, Nat. Mater. **13**, 241 (2014).
- [8] A. Mook, J. Henk, and I. Mertig, Phys. Rev. B **90**, 024412 (2014).
- [9] M. Mena, R. S. Perry, T. G. Perring, M. D. Le, S. Guerrero, M. Storni, D. T. Adroja, Ch. Rüegg, and D. F. McMorrow, Phys. Rev. Lett. **113**, 047202 (2014).
- [10] I. Lisenkov, V. Tyberkevych, A. Slavin, P. Bondarenko, B. A. Ivanov, E. Bankowski, T. Meitzler, and S. Nikitov, Phys. Rev. B **90**, 104417 (2014).
- [11] H. Lee, J. H. Han, and P. A. Lee, Phys. Rev. B **91**, 125413 (2015).
- [12] R. Chisnell, J. S. Helton, D. E. Freedman, D. K. Singh, R. I. Bewley, D. G. Nocera, and Y. S. Lee, Phys. Rev. Lett. **115**, 147201 (2015).
- [13] C.-E. Bardyn, T. Karzig, G. Refael, and T. C. H. Liew, Phys. Rev. B **93**, 020502(R) (2016).
- [14] S. A. Owerre, J. Phys.: Condens. Matter **28**, 386001 (2016).
- [15] R. Cheng, S. Okamoto, and D. Xiao, Phys. Rev. Lett. **117**, 217202 (2016).
- [16] V. A. Zyuzin and A.A. Kovalev, Phys. Rev. Lett. **117**, 217203 (2016).
- [17] S. K. Kim, H. Ochoa, R. Zarzuela, and Y. Tserkovnyak, Phys. Rev. Lett. **117**, 227201 (2016).
- [18] J. Fransson, A. M. Black-Schaffer, and A. V. Balatsky, Phys. Rev. B **94**, 075401 (2016).
- [19] F. Y. Li, Y. D. Li, Y. B. Kim, L. Balents, Y. Yu, and G. Chen, Nature Commun. **7**, 12691 (2016).
- [20] A. Mook, J. Henk, and I. Mertig, Phys. Rev. Lett. **117**, 157204 (2016).
- [21] Y. Su, X. S. Wang, and X. R. Wang, arXiv:1609.01500 (2016).
- [22] A. Mook, J. Henk, and I. Mertig, Phys. Rev. B. **95**, 014418 (2017).
- [23] X. S. Wang, Y. Su, and X. R. Wang, Phys. Rev. B. **95**, 014435 (2017).
- [24] S. O. Demokritov, and A. N. Slavin, *Magnonics: From Fundamentals to Applications* (Topics in Applied Physics Vol. 125, Springer, Berlin, 2013).
- [25] D. Grundler, Nat. Phys. **11**, 438 (2015).
- [26] B. Lenk, H. Ulrichs, F. Garbs, and M. Mnzenberg, Phys. Rep. **507**, 107 (2011).
- [27] A. V. Chumak, V. I. Vasyuchka, A. A. Serga, and B. Hillebrands, Nat. Phys. **11**, 453 (2015).
- [28] Y. Kajiwara, K. Harii, S. Takahashi, J. Ohe, K. Uchida, M. Mizuguchi, H. Umezawa, K. Kawai, K. Ando, K. Takanashi, S. Maekawa, and E. Saitoh, Nature (London) **464**, 262 (2010).
- [29] L. J. Cornelissen, J. Liu, R. A. Duine, J. B. Youssef, and B. J. van Wees, Nature Phys. **11**, 1022 (2015).
- [30] P. Yan, X. S. Wang, and X. R. Wang, Phys. Rev. Lett. **107**, 177207 (2011).
- [31] X. S. Wang, P. Yan, Y. H. Shen, G. E. W. Bauer, and X. R. Wang, Phys. Rev. Lett. **109**, 167209 (2012).
- [32] B. Hu and X. R. Wang, Phys. Rev. Lett. **111**, 027205 (2013).
- [33] Y. Aharonov and A. Casher, Phys. Rev. Lett. **53**, 319 (1984).
- [34] The various in-plane vectors in Fig. 1(a) are set as  $\mathbf{a}_1 = (0, -1, 0)$ ,  $\mathbf{a}_2 = (\sqrt{3}/2, 1/2, 0)$ ,  $\mathbf{a}_3 = (-\sqrt{3}/2, 1/2, 0)$ ,  $\mathbf{b}_1 = (\sqrt{3}/2, -3/2, 0)$ ,  $\mathbf{b}_2 = (\sqrt{3}/2, 3/2, 0)$ , and  $\mathbf{b}_3 = (-\sqrt{3}, 0, 0)$ , where the distance between nearest neighbor intralayer lattice sites is set as unity.
- [35] I. Dzyaloshinskii, J. Phys. Chem. Solids **4**, 241 (1958); T. Moriya, Phys. Rev. **120**, **91** (1960).
- [36] T. Holstein and H. Primakoff, Phys. Rev. **58**, 1098 (1940).
- [37] See Supplemental Material for magnon arcs, magnon bands, and surface spectral functions for the topological magnon insulator, type-II WM, and nodal-line magnon.
- [38] P. Hosur and X. L. Qi, C. R. Physique **14**, 857870 (2013).
- [39] H. B. Nielsen and M. Ninomiya, Phys. Lett. B **130**, 389 (1983).
- [40] X. Wan, A. M. Turner, A. Vishwanath, and S. Y. Savrasov, Phys. Rev. B **83**, 205101 (2011).
- [41] A. A. Soluyanov, D. Gresch, Z. Wang, Q. Wu, M. Troyer, X. Dai, and B. A. Bernevig, Nature (London) **527**, 495 (2015).
- [42] F. Meier and D. Loss, Phys. Rev. Lett. **90**, 167204 (2003); K. Nakata, J. Klinovaja, and D. Loss, arXiv:1611.09752 (2016).
- [43] X. R. Wang, Phys. Rev. B **53**, 12035 (1996).
- [44] A. Burkov, Science **350**, 378 (2015).
- [45] S. Y. Li, L. Taillefer, C. H. Wang, and X. H. Chen, Phys. Rev. Lett. **95**, 156603 (2005).
- [46] H. Z. Lu and S. Q. Shen, Front. Phys. **12**, 127201 (2017).

## Supplemental Material for Chiral Anomaly of Weyl Magnons in Stacked Honeycomb Ferromagnets

*Chern number.*—In order to elaborate the existence of topologically protected surface states in both Weyl magnon (WM) and topological magnon insulator phases, we calculate the Chern number in the  $k_x k_y$  plane from the Hamiltonian  $\mathcal{H}(\mathbf{k})$  used in the manuscript for fixed  $k_z$ 's. The Chern number as a function of  $k_z$  is

$$C(k_z) = \sum_{\eta=1,2} \frac{(-1)^\eta}{2} \text{sgn} \left[ (-1)^\eta 3\sqrt{3}D + K_- + J_- (1 - \cos k_z) \right]. \quad (\text{S1})$$

The Chern number changes from 0 to  $\pm 1$  and vice versa when the constant  $k_z$  plane pass through a Weyl node (WN) in momentum space. Therefore, the topologically protected surface states exist between WNs and the WNs are the starting or ending points of magnon arcs.  $C(k_z) \neq 0$  for all  $k_z$  in the topological magnon insulator phase, and topologically protected surface states exist in the magnon band gap.

*Magnon arc.*— For model parameters used in Fig. 2(b) and 2(c) of the manuscript, WNs of chirality  $\pm 1$  in the first bulk Brillouin zone (BZ) and their projection in the first (100) surface BZ are respectively denoted by the red and blue dots in Fig. S1(a) and S1(b), for the case of Fig. 2(b) and 2(c) in the manuscript. In order to see the magnon arcs formed from the topologically protected surface states near the WN energy on sample surfaces, we consider a slab of stacked honeycomb ferromagnets whose surfaces are perpendicular to the [100] direction, the same as that studied in the manuscript. For the model parameters used in Fig. 2(b) [or 2(e)] in the manuscript, there is one pair of WNs at  $\mathbf{k}_1^\pm$  on H'K'H' in the first bulk Brillouin zone (BZ) as shown in Fig. S1(a). For magnon energy  $\varepsilon = \varepsilon_1$  through the WNs, the calculated (100) surface spectral function is shown in the left panel of Fig. S1(c). Apparently, the surface states with high density (red color) on the top surface form magnon arcs that connect the two WNs  $\mathbf{k}_1^\pm$  of opposite chirality. The corresponding Chern number  $C(k_z)$  is computed and shown in the right panel of Fig. S1(c). Indeed  $C(k_{1,z}^- < k_z < k_{1,z}^+) = 1$  is consistent with the appearance of magnon arcs as shown in Fig. S1(c). For the model parameters used in Fig. 2(c) [or 2(f)] in the manuscript, there are two pairs of WNs at  $\mathbf{k}_1^\pm$  on H'K'H' and at  $\mathbf{k}_2^\pm$  on HKH in the first bulk BZ as shown in Fig. S1(b). Because the two pairs of WNs have difference energies  $\varepsilon_1$  and  $\varepsilon_2$ , we set the magnon energy  $\varepsilon = (\varepsilon_1 + \varepsilon_2)/2$  in the middle of the two pairs of WNs. The calculated (100) surface spectral function is shown in the left panel of Fig. S1(d). In the current case, the magnon arcs exist between WNs  $\mathbf{k}_1^+$  and  $\mathbf{k}_2^+$  of opposite chirality, and between WNs  $\mathbf{k}_1^-$  and  $\mathbf{k}_2^-$  of opposite chirality. The corresponding Chern number  $C(k_z)$  is shown in the right panel of Fig. S1(d) where  $C(k_{1,z}^- < k_z < k_{2,z}^-) = C(k_{2,z}^+ < k_z < k_{1,z}^+) = 1$  as expected.

*Topological magnon insulator.*—According to Eq. (S1),  $C(k_z) = 1$  in the topological magnon insulator phase [the Green region in Fig. S2(a)] for arbitrary  $k_z$ , while  $C(k_z) = 0$  in the trivial phase [the white regions in Fig. S2(a)] for

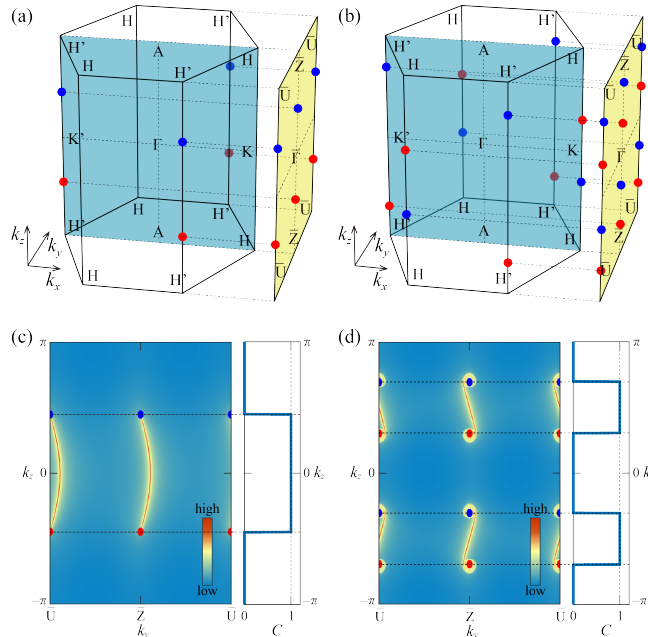


FIG. S1: (a) and (b) The first bulk Brillouin zone (BZ) and the first (100) surface BZ of stacked honeycomb lattices. The red and blue dots denote the Weyl nodes (WNs) of chirality  $\pm 1$  in Fig. 2(b) and 2(c) of the manuscript. (c) and (d) The density plot of the surface spectral functions on the first (100) surface BZ for model parameters used in Fig. 2(b) and 2(c) of the manuscript are shown in the left panels. The corresponding Chern numbers  $C(k_z)$  are shown in the right panels. The red curves between WNs are magnon arcs. The insets are colorbars

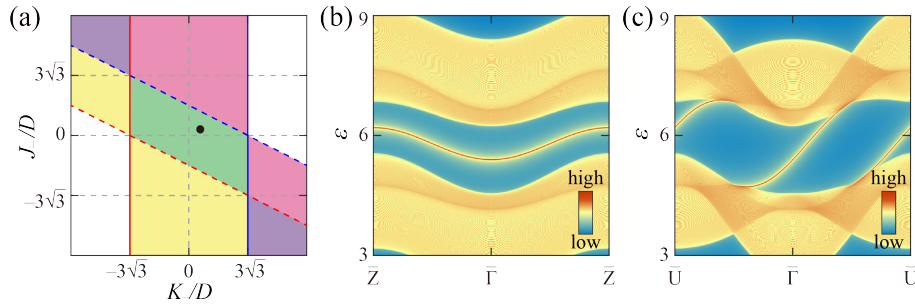


FIG. S2: (color online). (a) Phase diagram of stacked honeycomb ferromagnets in the  $K_-/D$ - $J_-/D$  plane. (b) and (c) The density plot of the (100) surface spectral function for the topological magnon insulator phase [the black dot in (a)] along  $\bar{Z}\bar{\Gamma}\bar{Z}$  (b) and along  $\bar{U}\bar{\Gamma}\bar{U}$  (c). Energy  $\varepsilon$  is in units of  $JS$ , and the insets are colorbars.

arbitrary  $k_z$ . To see the topologically protected surface states of the topological magnon insulator, we compute the (100) surface spectral function for the model parameters of  $D = 0.2J$ ,  $K_+ = 12D$ ,  $J_+ = 2D$ , and  $(K_-, J_-) = (D, 0.5D)$  marked by the black dot in Fig. S2(a) inside the topological magnon insulator phase. The density plot of the (100) surface spectral function along  $\bar{Z}\bar{\Gamma}\bar{Z}$  and along  $\bar{U}\bar{\Gamma}\bar{U}$  of the first (100) surface BZ are respectively shown in Fig. S2(b) and S2(c). As expected, the topologically protected surface states exist in the magnon band gap.

*Type-II WM and magnonic Landau level.*—In the manuscript we show that the WMs are of type-II when  $|J_+| > |J_-|$  according to the classification of Weyl semimetals [S1]. This can be easily seen from the effective Weyl Hamiltonian Eq. (3) of the manuscript in which the third term gives a Weyl cone while the second term tilts the Weyl cone along  $k_z$  direction in momentum space. According to the criteria of type-II Weyl semimetal in Ref. [S1], we obtain the condition for WMs becoming type-II in our model as  $|u_{\eta,z}^{\pm}| > |v_{\eta,z}^{\pm}| \Rightarrow |J_+| > |J_-|$ .

To confirm this result, we compute the magnon bands for the model parameters  $D = 0.2J$ ,  $K_+ = 12D$ ,  $(K_-, J_-) = (D, 5D)$  [indicated by the black dot in Fig. S3(a)], and  $J_+ = \{2D, 5D, 7D\}$ . In the current case, the WNs are located on the H'K'H' line in the first bulk BZ as shown in Fig. S1(a). Therefore, we plot magnon energy along H'K'H' and the results are shown in Fig. S3(b). Indeed, the system changes from the type-I WM to the type-II WM at  $J_+ = 5D = J_-$  where one magnon band is flat along the H'K'H' as shown in Fig. S3(b). For  $J_+ = 7D > J_-$ , it's clearly shown that the Weyl cones are tilted to be type-II.

Because the tilt of Weyl cone doesn't change its band topology, the topologically protected surface states should also exist between WNs in type-II WMs. In Fig. S3(c), we show the density plot of the (100) surface spectral function of the type-II WM with  $J_+ = 7D$  in Fig. S3(b) along  $\bar{Z}\bar{\Gamma}\bar{Z}$  of the first (100) surface BZ. Indeed the the tilted Weyl

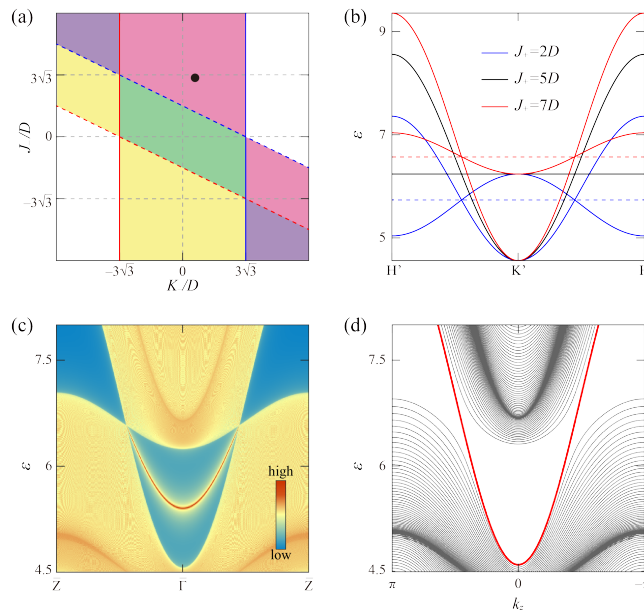


FIG. S3: (color online). (a) Phase diagram of stacked honeycomb ferromagnets in the  $K_-/D$ - $J_-/D$  plane. The various phases with different colors are explained in the manuscript. (b) Magnon bands for various  $J_+$  and other parameters corresponding to the black dot in (a) are plotted along the H'K'H' line. (c) The density plot of the (100) surface spectral function for the type-II WM with  $J_+ = 7D$  in (b) and along  $\bar{Z}\bar{\Gamma}\bar{Z}$ . The inset is the colorbar. (d) The MLLs of the type-II WM under an inhomogeneous electric field which is specified in the text. The red curve is the zeroth MLL, and  $\varepsilon$  is in units of  $JS$ .

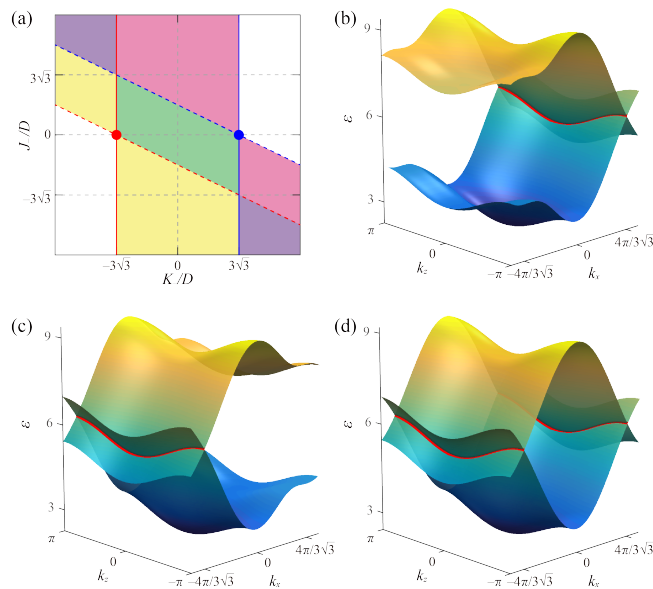


FIG. S4: (a) Phase diagram of stacked honeycomb ferromagnets in the  $K_-/D$ - $J_-/D$  plane. For the red and blue dots in (a), the magnon bands in the  $k_x k_z$  plane are shown in (b) and (c) in which band crossing occurs on a nodal line marked by the red curve. (d) The magnon bands for  $D = 0$  and  $K_- = 0$  with other parameters specified in the text. The band crossing occurs on two nodal lines.  $\varepsilon$  is in units of  $JS$ .

cone and surface states (red curve) are clearly identified.

According to the Aharonov-Casher effect [S2], magnons can interact with electric fields that results in magnonic Landau levels (MLLs) as described in the manuscript. Here we consider the type-II WM coupled to an inhomogeneous electric field  $\mathbf{E} = (\mathcal{E}x, 0, 0)$  with  $\mathcal{E} = 1/100\sqrt{3}$  in units of  $\hbar c^2/g\mu_B$ . The MLLs of the type-II WM are shown in Fig. S3(d) and the zeroth MLL is the red curve. The zeroth MLL is still chiral but cannot be separated from higher MLLs, because there is no band gap between the first MLLs.

*Nodal-line magnon.*—At  $(K_-/D, J_-/D) = (-3\sqrt{3}, 0)$  [the red dot in Fig. S4(a)] and  $(3\sqrt{3}, 0)$  (the blue dot), WMs becomes nodal-line magnons whose two magnon bands cross on HKH line for the former and on H'K'H' line for the later as mentioned in the manuscript. In order to visualize these nodal lines, we calculate the magnon bands for the red and blue dots in Fig. S4(a) with the other model parameters  $D = 0.2J$ ,  $K_+ = 12D$ , and  $J_+ = 2D$ . The energy surfaces of two bands as a function of  $k_x$  and  $k_z$  for fixed  $k_y = 0$  [the blue plane in Fig. S1(a)] are plotted in Fig. S4(b) (for the red dot) and S4(c) (for the blue dot). The nodal lines are marked by red curves. When  $K_- = D = 0$  (with the other parameters unchanged), the red and blue dots merge together and the two nodal lines coexist as shown in Fig. S4(d).

[S1] A. A. Soluyanov, D. Gresch, Z. Wang, Q. Wu, M. Troyer, X. Dai, and B. A. Bernevig, Nature (London) **527**, 495 (2015).

[S2] Y. Aharonov and A. Casher, Phys. Rev. Lett. **53**, 319 (1984).